

## Satellite-based assessment of marine low cloud variability associated with aerosol, atmospheric stability, and the diurnal cycle

Toshihisa Matsui,<sup>1</sup> Hirohiko Masunaga,<sup>1</sup> Sonia M. Kreidenweis,<sup>1</sup> Roger A. Pielke Sr.,<sup>1</sup> Wei-Kuo Tao,<sup>2</sup> Mian Chin,<sup>2</sup> and Yoram J. Kaufman<sup>2</sup>

Received 16 April 2005; revised 21 April 2006; accepted 16 May 2006; published 9 September 2006.

[1] This study examines variability in marine low cloud properties derived from semiglobal observations by the Tropical Rainfall Measuring Mission (TRMM) satellite, as linked to the aerosol index (AI) and lower-tropospheric stability (LTS). AI is derived from the Moderate Resolution Imaging Spectroradiometer (Terra MODIS) sensor and the Goddard Chemistry Aerosol Radiation and Transportation (GOCART) model and is used to represent column-integrated aerosol concentrations. LTS is derived from the NCEP/NCAR reanalysis and represents the background thermodynamic environment in which the clouds form. Global statistics reveal that cloud droplet size tends to be smallest in polluted (high-AI) and strong inversion (high-LTS) environments. Statistical quantification shows that cloud droplet size is better correlated with AI than it is with LTS. Simultaneously, the cloud liquid water path (CLWP) tends to decrease as AI increases. This correlation does not support the hypothesis or assumption that constant or increased CLWP is associated with high aerosol concentrations. Global variability in corrected cloud albedo (CCA), the product of cloud optical depth and cloud fraction, is very well explained by LTS, while both AI and LTS are needed to explain local variability in CCA. Most of the local correlations between AI and cloud properties are similar to the results from the global statistics, while weak anomalous aerosol-cloud correlations appear locally in the regions where simultaneous high (low) AI and low (high) LTS compensate each other. Daytime diurnal cycles explain additional variability in cloud properties. CCA has the largest diurnal cycle in high-LTS regions. Cloud droplet size and CLWP have weak diurnal cycles that differ between clean and polluted environments. The combined results suggest that investigations of marine low cloud radiative forcing and its relationship to hypothesized aerosol indirect effects must consider the combined effects of aerosols, thermodynamics, and the diurnal cycle.

**Citation:** Matsui, T., H. Masunaga, S. M. Kreidenweis, R. A. Pielke Sr., W.-K. Tao, M. Chin, and Y. J. Kaufman (2006), Satellite-based assessment of marine low cloud variability associated with aerosol, atmospheric stability, and the diurnal cycle, *J. Geophys. Res.*, *111*, D17204, doi:10.1029/2005JD006097.

### 1. Introduction

[2] Global low cloud properties critically control the Earth's radiation budget and hydrological cycle. Marine low clouds have been extensively observed in the descending branch of the Hadley Circulation, where large-scale subsidence occurs [Klein and Hartmann, 1993]. Marine low clouds have an annually and globally averaged net cooling effect of  $-15$  ( $\text{W}/\text{m}^2$ ) [Hartmann *et al.*, 1992]. A 4% increase in low cloud cover could offset the anthropogenic greenhouse gas warming due to a doubling of  $\text{CO}_2$  [Slingo, 1990]. The *National Research Council* [2005] highlighted

the importance of cloud radiative effects within the climate system. Variability in global low cloud fields modulates the warm rain rate, which is estimated to account for 31% of the total surface precipitation over the tropics [Lau and Wu, 2003]. This large effect on the Earth's climate prompts scientists to examine the variability of low cloud properties as linked to various meteorological parameters, such as sea surface temperature (SST), relative humidity (RH) near cloud layers, and lower-tropospheric stability (LTS) [e.g., Weare, 1994; Klein and Hartmann, 1993; Park and Leovy, 2004; Klein, 1997]. Comparisons of different parameters used in cloud models show that no single meteorological parameter explains more than 13% of the variance in low-cloud amounts, and that multiple regressions using a combination of different parameters do not increase the explained variance [Klein, 1997].

[3] Marine low clouds have a strong diurnal cycle due to radiation-driven turbulence in the cloud-capped marine boundary layer [e.g., Driedonks and Duijkerke, 1989]. In

<sup>1</sup>Department of Atmospheric Science, Colorado State University, Fort Collins, Colorado, USA.

<sup>2</sup>Laboratory for Atmospheres, NASA Goddard Space Flight Center, Greenbelt, Maryland, USA.

the early morning, solar radiation starts heating the subcloud layer, while longwave emission cools the cloud top. The combination of longwave cooling and shortwave heating drives turbulent mixing that (1) destabilizes the cloud layer separately from the rest of the boundary layer and (2) induces entrainment of dry air that thins the cloud layer in a complex manner. The isolated layer progressively thins the cloud during the late morning and into the afternoon (see the review given by *Driedonks and Duynkerke* [1989]). This diurnal cloud cycle was captured in the Atlantic Stratocumulus Transition Experiment (ASTEX) [*Cieselski et al.*, 2001], in the First International Satellite Cloud Climatology Project Regional Experiment (FIRE) [*Hignett*, 1991], and in observations from the California coastal region [*Betts*, 1990]. *Wood et al.* [2002] showed the semi-global-scale diurnal cycle of the cloud liquid water path (CLWP) using a 2-year data set from the Tropical Rainfall Measuring Mission (TRMM) satellite. They demonstrated that the diurnal cycle generally peaked early in the morning, but that the timing of those peaks varied slightly in different geographic regions.

[4] In recent decades, advanced space-borne satellites and global modeling systems investigated the global distribution of aerosol concentrations [*Kaufman et al.*, 2002]. Hygroscopic aerosol particles serve as cloud condensation nuclei (CCN) that initiate the formation of cloud droplets. Higher concentrations of submicron aerosols are expected to reduce the average size of cloud droplets, in turn increasing the cloud albedo under the assumption of constant liquid water content [*Twomey et al.*, 1984], and could enhance the cloud liquid water path by inhibiting the precipitation initiation process [*Albrecht*, 1989]. These aerosol-cloud-climate linkages are called the aerosol indirect effects. Many studies show a reduction of cloud droplet size associated with high aerosol concentrations observed in ground-based experiments [e.g., *Feingold et al.*, 2003; *Penner et al.*, 2004] as well as in satellite imagery [e.g., *Kaufman and Fraser*, 1997; *Nakajima et al.*, 2001; *Bréon et al.*, 2002; *Matsui et al.*, 2004a; *Kaufman et al.*, 2005]. Some of the studies capture rainfall inhibition due to air pollution [*Rosenfeld*, 1999; *Matsui et al.*, 2004a]. Although many researchers show links between small cloud droplets and high aerosol concentrations in the ambient air, they do not consistently find a dramatic increase in cloud albedo as initially hypothesized, probably because of the complicated feedbacks involving thermodynamics and below-cloud turbulent mixing processes [*Jiang et al.*, 2002].

[5] Another important aspect of the aerosol effect is that aerosol particles absorb and scatter radiation, which is denoted as the aerosol direct effect. Absorbing aerosols, such as black carbon and mineral dust, could contribute to high diabatic heating in the atmosphere that often enhances cloud evaporation (the semidirect effect) [*Ackerman et al.*, 2000; *Koren et al.*, 2004; *Krüger and Graßl*, 2004]. Atmospheric diabatic heating could strengthen inversions, which could inhibit the cyclogenesis process and consequently constrain hurricane tracks [*Dunion and Velden*, 2004]. *Ramanathan et al.* [2001] suggested that a combination of the aerosol direct and indirect effects could weaken the hydrological cycle, which could be a major environmental issue in this century.

[6] To summarize, the large-scale thermodynamic field, the radiation-driven diurnal cycle, and aerosol-cloud interactions are all critical in understanding the variability of global marine low cloud properties. This study attempts to incorporate these aspects together to arrive at a deeper understanding of marine low cloud variability. This study extends the analysis by *Matsui et al.* [2004a] to an annual cycle (section 2), includes different aerosol data sets (section 2.1), examines not only cloud droplet size but also cloud liquid water path and cloud albedo (section 2.3), statistically quantifies the relationship on the global scale (section 3.1) and local scale (section 3.2), and examines the diurnal cycle in regions with different thermodynamic environments and aerosol concentrations (section 3.3).

## 2. Data Sets and Method

### 2.1. Lower-Tropospheric Stability (LTS) From the NCEP/NCAR Reanalysis

[7] A large amount of latent heat release over the warm sea surface drives upward motion in the equatorial regions and large-scale subsidence in the subtropics. The large-scale subsidence over cold sea surface temperatures (SST) creates a strong inversion in the lower troposphere. Consequently, cool, moist air below the inversion layer supports an increase in the relative humidity (RH) and, thus, frequent cloudiness. The magnitude of the inversion strength can be measured as the potential temperature difference between the atmosphere at the 700-mb level and the surface, denoted as lower-tropospheric stability (LTS) [*Klein and Hartmann*, 1993].

[8] *Klein* [1997] found that LTS is highly correlated with cloud amount, although other parameters such as lower-tropospheric relative humidity are important as well. This study focuses on LTS as an indicator of the thermodynamic environment, as was done in the previous study [*Matsui et al.*, 2004a], where low-cloud properties were investigated in terms of aerosols and LTS. While the role of other parameters is certainly important, their impact on low clouds is not considered in the present paper, as we wanted to focus specifically on LTS. LTS is also more readily derived from remote sensing soundings or objective analyses, in comparison with subgrid parameters, such as cloud updraft velocity or turbulent kinetic energy. In this study, LTS is derived from the NCEP/NCAR reanalysis data set ( $2.5^\circ \times 2.5^\circ$  grid space) [*Kalnay et al.*, 1996]. Although LTS can be correlated with aerosols on the regional scale, these correlations tend to be canceled out on the global scale. For example, global linear correlations between AI and LTS are  $-0.016$  and  $0.024$  for the MODIS and GOCART cases, respectively. These values are significant at 0.05 level, but are very small. Regional correlations of LTS with AI can account for regional anomalies in the dependence of cloud properties on AI and LTS, as discussed later.

[9] Figure 1 shows the annual mean and standard deviation of the global distribution of LTS sampled from March 2000 to February 2001 at the same sampling rate as that of the cloud data set. LTS varies season-by-season and year-by-year. Regions with high LTS (strong inversions) are frequently observed off the coast of California, Namibia, and Chile. Those areas are located in the eastern parts of major oceans (Figure 1). Low-LTS regions are found in the

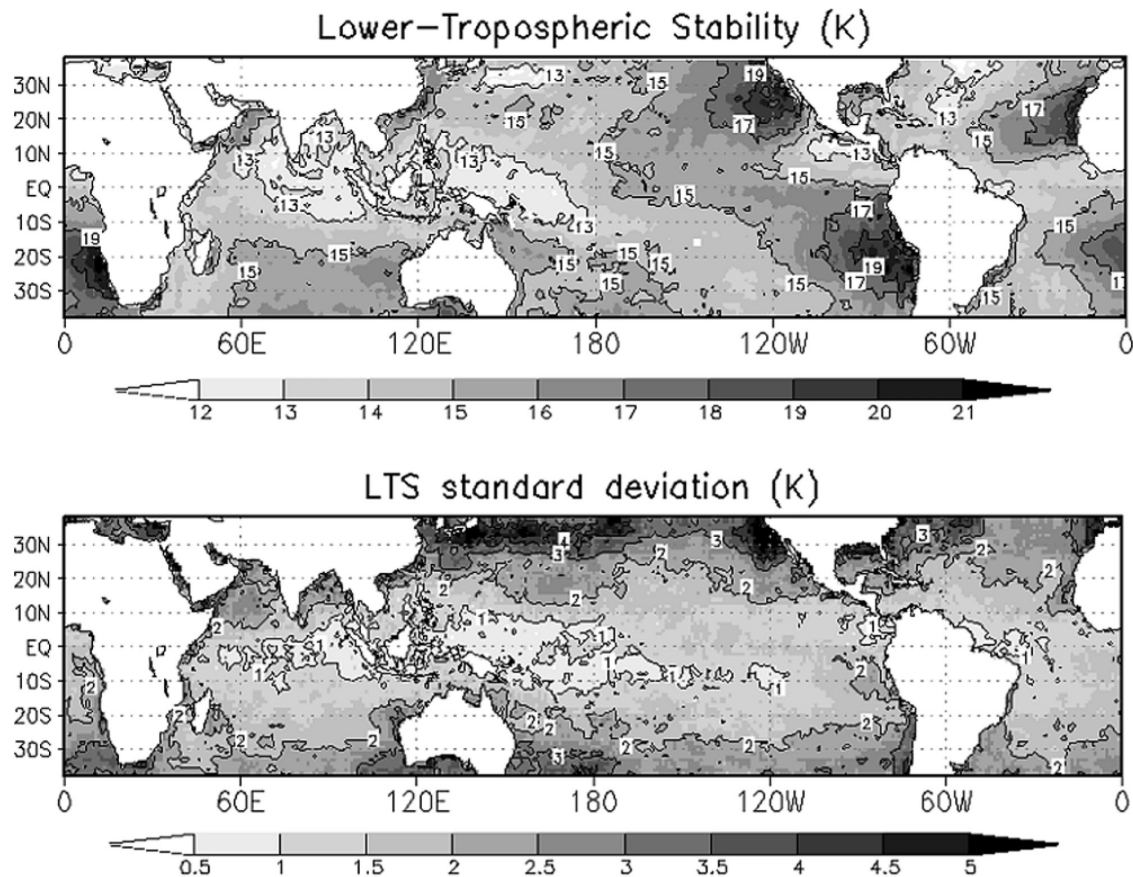


**Figure 1.** (top) Annual mean and (bottom) standard deviation of lower-tropospheric stability (LTS), sampled from March 2000 to February 2001. High-LTS (strong inversion) regions are located in the eastern parts of major oceans.

tropics over warm SSTs, where surface energy flux and mass convergence create strong vertical mixing in the boundary layer. LTS exhibits large standard deviations in midlatitude regions, in comparison to those in seen in the tropics (Figure 1), because of propagating synoptic fronts and seasonal shifts of the Hadley cell.

## 2.2. Aerosol Index From MODIS and GOCART

[10] In this study, aerosol concentration is represented by the Aerosol Index (AI), which is the product of aerosol optical depth (AOD) and the Ångström exponent. AI is better correlated with column aerosol concentrations and cloud properties than is AOD alone [Nakajima *et al.*, 2001; Bréon *et al.*, 2002]. Global aerosol distributions from satellite retrievals and global chemistry transport model calculations are used in this study, since both data have different advantages and disadvantages [Yu *et al.*, 2003; Chin *et al.*, 2004; Matsui *et al.*, 2004b]. The satellite data set used to compute AI is the Moderate Resolution Imaging Spectroradiometer (Terra MODIS) Level-3 (collection 4) instantaneous AOD at 0.55  $\mu\text{m}$  and Ångström exponent between 0.55  $\mu\text{m}$  and 0.87  $\mu\text{m}$ , which are archived on a global  $1^\circ \times 1^\circ$  latitude-longitude grid. A comprehensive description of the algorithm, sensor specification, validation, and data sets is summarized by Remer *et al.* [2005]. The other data set used to compute AI is from the Goddard Chemistry Aerosol Radiation and Transportation

(GOCART) model, which is a global chemical-aerosol-transport model driven by the Goddard Earth Observing System Data Assimilation System (GEOS DAS) global analysis ( $2^\circ \times 2.5^\circ$  grid space). It prognoses a global distribution of sulfate and its precursors, organic carbon, black carbon, mineral dust, and sea salt (see details given by Chin *et al.* [2002, 2004]). This study computes AI from GOCART predictions of daily AOD at 0.55  $\mu\text{m}$  and Ångström exponent between 0.55  $\mu\text{m}$  and 0.90  $\mu\text{m}$ . The Ångström exponent ( $-\frac{d \log AOD}{d \log \lambda}$ , where  $\lambda$  is the wavelength at which AOD is determined) is an indicator of the size distribution of aerosols; e.g., fine-mode particulate matter, such as sulfate and organic carbon, tend to be associated with high Ångström exponents, whereas the size distributions of coarse-mode particles, such as large sea salt and dust, tend to have low (near-zero) Ångström exponents.

[11] While satellite estimates of AOD are based on the measured instantaneous top-of-atmosphere (TOA) radiance, estimates of AOD from global chemistry transport models are calculated on the basis of aerosol and precursor emissions inventories, atmospheric objective analysis, and simulated aerosol optical and microphysical properties. Intercomparison of AOD at 0.55  $\mu\text{m}$  between MODIS retrievals and GOCART simulations has been reported for global and regional scales [Yu *et al.*, 2003; Chin *et al.*, 2004; Matsui *et al.*, 2004b]. Figure 2a shows the global distribution of GOCART and MODIS AI integrated from 1 March

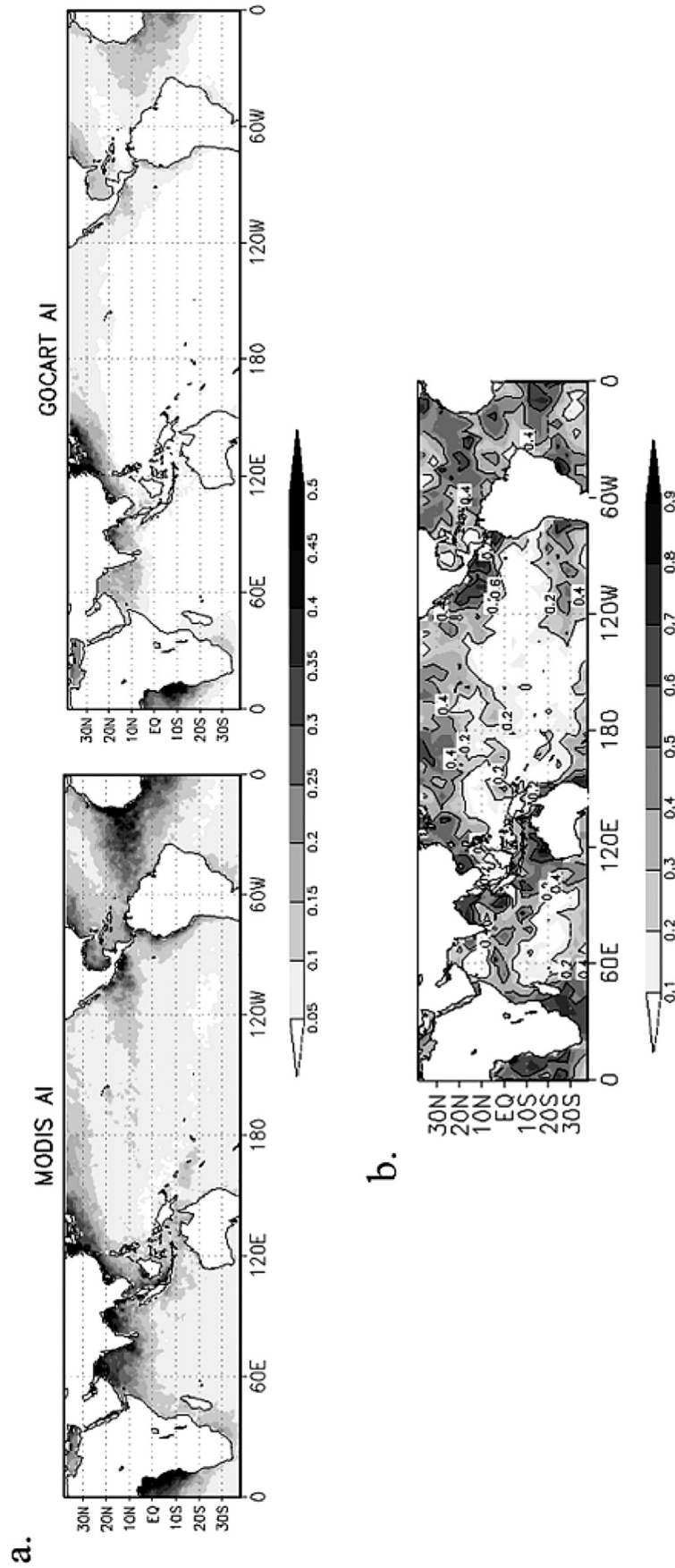


**Figure 2.** (a) Annual average of MODIS and GOCART AI. (b) Local linear correlation coefficient (in  $4^\circ \times 4^\circ$  grid boxes) between daily GOCART AI and MODIS AI. All data are sampled from March 2000 to February 2001.

2000 to 28 February 2001, whenever MODIS retrievals and GOCART outputs are simultaneously available. MODIS and GOCART AI exhibit high spatial coherence on global scales (correlation: 0.83). High values of AI appear along the coastlines of Asia, India, eastern United States, and West Africa. Very small values of AI appear in the remote Indian and Pacific Oceans. However, local correlations (daily correlation in  $4^\circ \times 4^\circ$  grid boxes) are highly variable in different regions (Figure 2b). Remote oceans, particularly the southern portions of the Indian and Pacific Oceans, have correlations less than 0.2 between MODIS and GOCART AI, probably because of the low, and therefore more uncertain, AI values.

[12] The GOCART model explicitly simulates different aerosol species in four-dimensional fields. When we convert the GOCART-predicted AOD to AI, the summation of the contributions of sulfate, organic carbon, and black carbon represents approximately 97% of the total AI. Dust and sea salt together represent about 3% of the total AI, because the Ångström exponents of the assumed size distributions for those species are close to zero. Large particles of sea salt and sulfate-coated dust serve as giant cloud condensation nuclei (GCCN). GCCN potentially enhance the cloud drizzle process in environments characterized by high CCN concentrations, but probably have little effect in low-CCN-concentration environments where drizzle is active regardless of the presence of GCCN [Feingold *et al.*, 1999]. However, it is not possible using AI to explicitly investigate the potential role of GCCN, as investigated by Feingold *et al.* [1999]. Emissions of sulfate and sulfate precursors and of organic carbon are primarily from industrial and agricultural activities. Therefore AI derived from multispectral AOD allows us to focus on the anthropogenic aerosol impact on marine low cloud. Although the size distributions assumed in the MODIS retrievals are slightly different from those used in GOCART, the correspondence between aerosol types and concentrations and MODIS AI can be similarly interpreted.

[13] The vertical distribution of AI remains uncertain in satellite-based aerosol-cloud interaction studies [Matsui *et al.*, 2004a; Bréon *et al.*, 2002; Nakajima *et al.*, 2001; Sekiguchi *et al.*, 2003]. More accurate assessments will be available when the multisatellite A-Train platform is established [Stephens *et al.*, 2002; Kaufman *et al.*, 2003].

### 2.3. Marine Low Cloud Properties From the TRMM Satellite

[14] Masunaga *et al.* [2002a] proposed a new algorithm that simultaneously derives different cloud properties through a combined use of data from the TRMM Microwave Imager (TMI) and Visible/Infrared Radiance Imager (VIRS). First, VIRS radiances at 0.63 micron, 3.7 micron, and 10.8 micron are used to derive low-cloud optical depths, cloud top droplet effective radius (Re(top)), and cloud top temperature [Kawamoto *et al.*, 2001; GTR 1.0 package from T. Y. Nakajima, personal communication, 2003]. Second, TMI brightness temperatures at 10.65 GHz, 19.35 GHz, and 37.0 GHz yield the column water vapor and cloud liquid water path (CLWP) for the VIRS-derived cloud top temperatures and cloud fractions. We updated the look-

up table used by the microwave algorithm so that it allows realistic variability of the water vapor and temperature profiles to improve the products obtained by Masunaga *et al.* [2002a] and Matsui *et al.* [2004a]. The TMI-derived CLWP ( $CLWP_{TMI}$ ) with the VIRS-derived optical thickness ( $\tau_{VIRS}$ ) provide the cloud droplet effective radius (Re) via

$$Re(column) = \frac{1.5 CLWP_{TMI}}{\rho_w \tau_{VIRS}},$$

where  $\rho_w$  represents water density. Re(column) represents column-integrated Re, since microwave brightness temperature and visible radiance do not suffer from saturation within any cloud thickness of marine low clouds (see the details of the algorithm given by Masunaga *et al.* [2002a]). Simultaneous analysis of Re(top) and Re(column) provides more information to examine warm rain processes [Masunaga *et al.*, 2002b; Matsui *et al.*, 2004a].

[15] Klein and Hartmann [1993] showed that the low-cloud fraction is the primary parameter controlling the surface cooling effect. While many studies focus on the change in cloud optical depth and cloud fraction separately, this study uses cloud amount defined by the corrected cloud albedo, CCA:

$$CCA = A_{cloud} * CF,$$

where CF is the low-cloud fraction in a  $1 \times 1^\circ$  box derived from VIRS 2km-footprint pixels, and  $A_{cloud}$  is the cloud albedo, which is expressed for a plane-parallel cloud in a two-stream radiative transfer model [Hobbs, 1993] as,

$$A_{cloud} = \frac{\tau_{VIRS}}{\tau_{VIRS} + 6.7}.$$

CCA accounts for cloud radiative forcing as the combined effect of the cloud optical depth and cloud fraction.

[16] To define a VIRS 2km-footprint pixel that is overcast, the following criteria must be satisfied simultaneously [Kawamoto *et al.*, 2001]: (1) Radiances in channel 1 ( $\lambda = 0.623 \mu\text{m}$ ), channel 2 ( $\lambda = 1.610 \mu\text{m}$ ), and channel 3 ( $\lambda = 3.784 \mu\text{m}$ ) are all positive; (2) solar zenith angle must be within  $0 \sim 60^\circ$ ; (3) reflectance in channel 1 is greater than the sum of 0.1 and the ocean albedo value; (4) brightness temperature of channel 4 ( $\lambda = 10.826 \mu\text{m}$ ) is less than the sea surface temperature; (5) brightness temperature of channel 4 ( $\lambda = 10.826 \mu\text{m}$ ) is greater than brightness temperature of channel 5 ( $\lambda = 12.028 \mu\text{m}$ ); and (6)  $3 \times 3$ -window standard deviations of channel 1 is less than  $100 \text{ Wm}^{-2} \text{ster}^{-1} \mu\text{m}^{-1}$ , and  $3 \times 3$ -window standard deviations of brightness temperature of channel 5 is also less than 100 K, indicating a horizontally homogeneous pixel. Cloud pixels with high ambient aerosols were removed from the analysis by taking the 95% of the total PDF (Figure 3). These data screening procedures should ensure

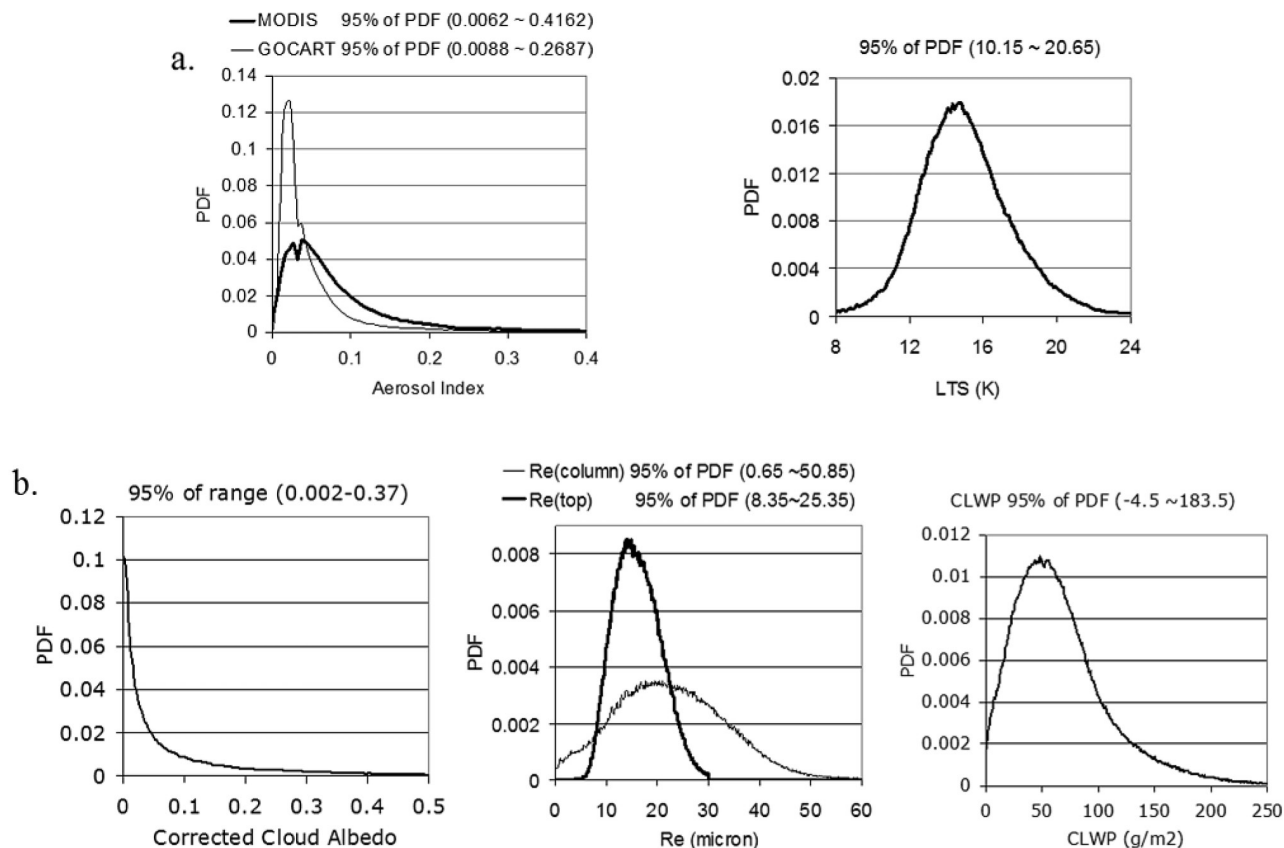


**Figure 3.** Probability density function (PDF) of (a) AI and LTS and (b) cloud properties. Variability of 95% of the total PDF is shown for each variable.

separation between cloudy pixels and pixels with very high aerosol concentrations.

#### 2.4. Method of Analysis

[17] This section describes the various statistical method and results. The sampling and statistical methods are as follows.

[18] 1. Sample the TRMM-derived low cloud properties, MODIS AI, GOCART AI, and NCEP LTS, only when they are simultaneously available. Note that the NCEP LTS is temporally interpolated to coincide with the TRMM satellite overpasses. MODIS AI values are instantaneous values at approximately 10:30 am local time, and GOCART AI values are daily averages. Although a time lag up to  $\pm 5$  hour exists between the MODIS and TRMM overpasses, temporal autocorrelations of aerosol extinction are still very high in this range [Anderson *et al.*, 2003].

[19] 2. Generate the probability density function (PDF) of MODIS AI, GOCART AI and NCEP LTS from the total samples (Figure 3).

[20] 3. Select 95% of the most frequent ranges from the total PDF by removing  $\pm 2.5\%$  of the smallest and largest values for MODIS AI, GOCART AI and NCEP LTS. For a normal distribution, 95% of the total PDF is equivalent to the range of four standard deviations ( $4\sigma$ ). These ranges are represented as  $dAI_{95\%}$  (0.41 for MODIS; 0.26 for GOCART) and  $dLTS_{95\%}$  (10.5K), respectively (Figure 3).

[21] 4. Similarly, select 95% of the most frequent ranges for  $Re(column)$ , CLWP, and CCA. These ranges are

represented as  $dRe(column)_{95\%}$  (50.0  $\mu\text{m}$ ),  $dCLWP_{95\%}$  (188.0  $\text{g}/\text{m}^2$ ), and  $dCCA_{95\%}$  (0.37) (Figure 3). These values are used to examine how well AI and LTS can explain the variability of cloud properties.

[22] 5. Select the sampling bins for MODIS AI, GOCART AI and NCEP LTS as 10% of  $dAI_{95\%}$  and  $dLTS_{95\%}$ , respectively. These are represented as  $dAI_{bin}$  (0.04 for MODIS; 0.026 for GOCART) and  $dLTS_{bin}$  (1.05 K).

[23] 6. Compute mean values of  $Re(column)$ , CLWP, and CCA for each bin ( $dAI_{bin}$  and  $dLTS_{bin}$ ) of the MODIS AI, GOCART AI and NCEP LTS. Mean values are represented as  $\overline{Re(column)}$ ,  $\overline{CLWP}$ , and  $\overline{CCA}$ .

[24] The above symbols and variables are summarized in the Notation section. The TRMM overpasses include the annual cycle from March 2000 to February 2001. Sampling is significantly concentrated in the subtropics because of the large amount of marine low cloud in those regions and the unique overpass pattern of the TRMM satellite (Figure 4). The sampling weights are identical between the GOCART and MODIS cases. Sampling was restricted to low clouds, defined as those which have a cloud top temperature above 273 K.

[25] It is worthwhile to note that  $Re(top)$  is generally larger than  $Re(column)$  for nonprecipitating clouds, while  $Re(top)$  can be smaller than  $Re(column)$  for precipitating clouds [Masunaga *et al.*, 2002a; Matsui *et al.*, 2004a]. Figure 3b shows the mode of  $Re(column)$  appear to be

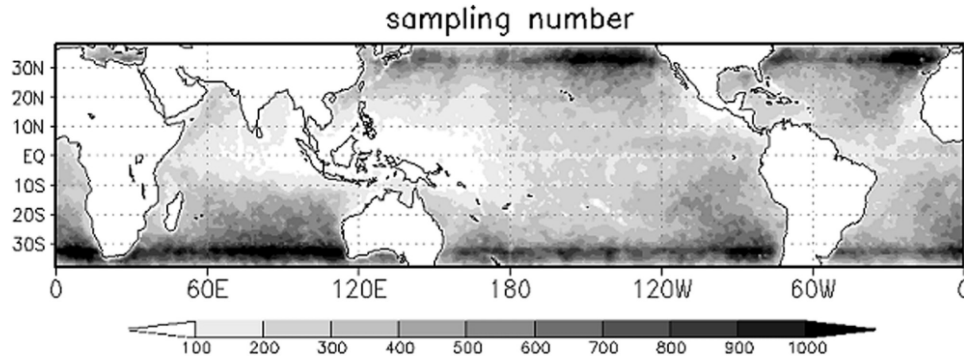


**Figure 4.** Global distribution of sampling number. Sampling numbers are significantly concentrated in the subtropics because of the large amount of marine low cloud and the unique overpass pattern of the TRMM satellite.

greater than the  $\overline{Re(top)}$ . This is possibly explained by the sampling biases in precipitating clouds and/or algorithm biases. We must reexamine  $\overline{Re(column)}$ - $\overline{Re(top)}$  relationship and algorithm for different types of clouds in different climatological regions, when the global-scale vertical profile of cloud properties become available [Stephens *et al.*, 2002]. Nevertheless, this uncertainty fundamentally does not affect our analysis, since this study does not focus on the comparison between  $\overline{Re(top)}$  and  $\overline{Re(column)}$ .

### 3. Results

#### 3.1. Global Statistics Among Cloud Properties, LTS, and AI

[26] Figure 5a shows the variability of  $\overline{Re(column)}$  as a function of  $LTS$  and  $AI$ . Clean (low- $AI$ ) environments in regions with low  $LTS$  tend to have the largest  $\overline{Re(column)}$ , while polluted (high- $AI$ ) environments with high  $LTS$  tend to have the smallest  $\overline{Re(column)}$ . Table 1 shows the changes in cloud properties for  $dAI_{95\%}$  and  $dLTS_{95\%}$ . For example,  $d\overline{Re(column)}_{95\%}$  for  $dAI_{95\%}$  and  $dLTS_{95\%}$  are defined as

$$d\overline{Re(column)}_{95\%} = \frac{\sum_{LTSbin} \left( \overline{Re(column)}_{low\_AIbin} - \overline{Re(column)}_{high\_AIbin} \right) * sampling\#_{LTSbin}}{\sum_{LTSbin} sampling\#_{LTSbin}} \quad (1)$$

$$\frac{\sum_{AIbin} \left( \overline{Re(column)}_{low\_LTSbin} - \overline{Re(column)}_{high\_LTSbin} \right) * sampling\#_{AIbin}}{\sum_{AIbin} sampling\#_{AIbin}}$$

where  $\overline{Re(column)}_{low\_AIbin}$  is the  $\overline{Re(column)}$  in the lowest bin of  $AI$ ,  $\overline{Re(column)}_{high\_AIbin}$  is the  $\overline{Re(column)}$  in the highest bin of  $AI$ ,  $\overline{Re(column)}_{low\_LTSbin}$  is the  $\overline{Re(column)}$  in the lowest bin of  $LTS$ , and  $\overline{Re(column)}_{high\_LTSbin}$  is the  $\overline{Re(column)}$  in the highest bin of  $LTS$ . Similar definitions are applied to CLWP and CCA.

[27] This result shows that an increase in  $dAI_{95\%}$  corresponds to a reduction of  $12.24 \mu m$  in  $\overline{Re(column)}$  in the MODIS case and  $12.19 \mu m$  in the GOCART case, explaining 24.4% and 24.3% respectively of  $d\overline{Re(column)}_{95\%}$  ( $50.0 \mu m$ ) (Table 1). Similarly, an increase in  $dLTS_{95\%}$  corresponds to a reduction of  $8.77 \mu m$  in  $\overline{Re(column)}$  in the MODIS case and  $8.35 \mu m$  in the GOCART case, explaining

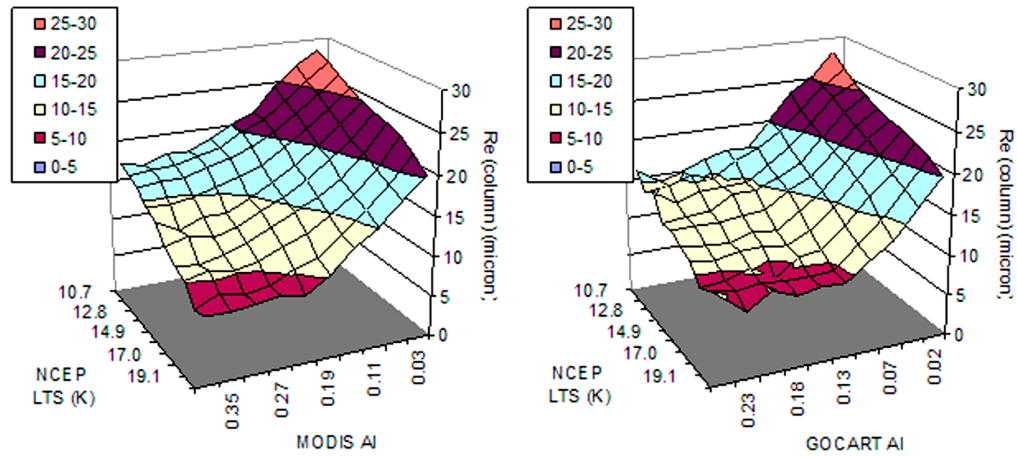
17.5% and 16.6% respectively of  $d\overline{Re(column)}_{95\%}$  ( $50.0 \mu m$ ) (Table 1). Note that relationships between  $LTS$  and cloud properties appear to be slightly different between the MODIS and GOCART cases, although  $LTS$  is independent of  $AI$  in the global sampling. This is because differences in global distribution of  $AI$  between MODIS and GOCART cause slightly different sampling of background  $LTS$ . In both cases, however, the global distribution of cloud droplet size is correlated better with  $AI$  than it is with  $LTS$ . This result can be applied to the warm rain process, since the process can be diagnosed by the droplet effective size [Matsui *et al.*, 2004a].

[28] Figure 5a shows that the relationships between  $\overline{Re(column)}$  and  $AI$  are nonlinear, whereas the  $\overline{Re}$ - $LTS$  slopes are approximately linear. For example,  $\overline{Re(column)}$  appears to decline more rapidly with increases in  $AI$  for small  $AI$ , whereas increases in  $AI$  at high  $AI$  do not reduce the cloud droplet size effectively. This trend for small  $AI$  is important, because small values of  $AI$  are much more frequent than high values (Figure 3a). Thus we additionally define changes in  $\overline{Re(column)}$  between neighboring bins

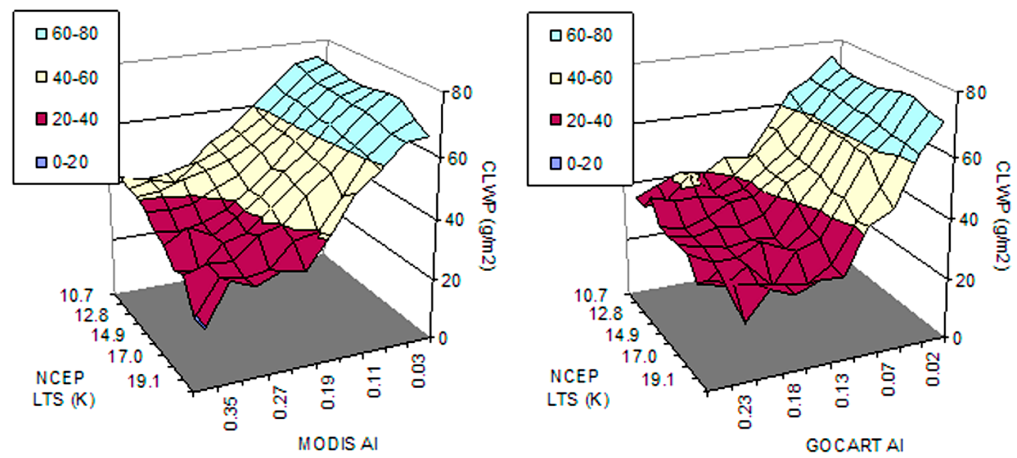
( $dAI_{bin}$  and  $dLTS_{bin}$ ), weighted by the frequency distribution of the sampling number, which is strongly peaked near the mean value of the  $LTS$  PDF and low  $AI$  values (Figure 3a):

$$d\overline{Re(column)}_{freq} = \frac{\sum_{LTSbin} \sum_{AIbin} d\overline{Re(column)} * sampling\#_{bin}}{\sum_{LTSbin} \sum_{AIbin} sampling\#_{bin}} \quad (2)$$

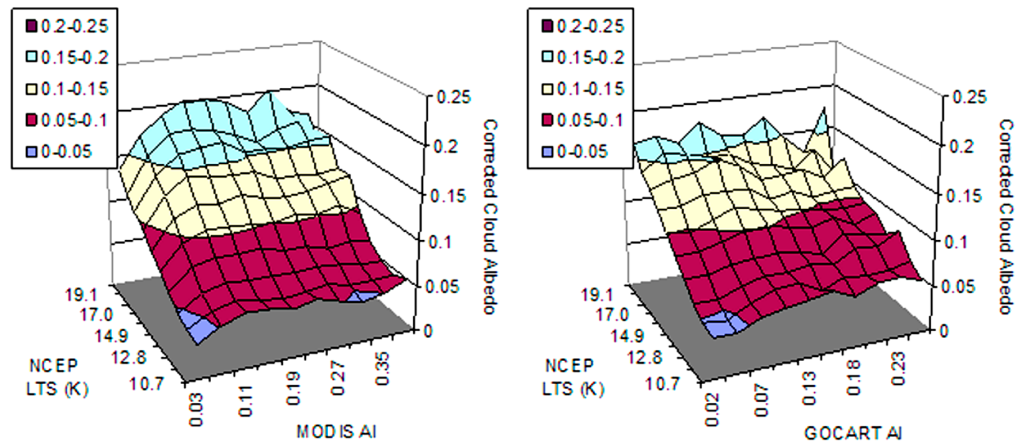
The similar definition is applied to CLWP and CCA. This value represents the frequency weighted mean values of the change in clouds properties over the globe. Table 2 shows  $d\overline{Re(column)}_{freq}$  ( $-1.80$  and  $-0.94$ , respectively) as a function of  $dAI_{bin}$  and  $dLTS_{bin}$ .  $dAI_{bin}$  explains twice the



a. Column cloud droplet effective radius



b. Cloud liquid water path



c. Corrected cloud albedo (cloud amount)

**Figure 5.** Global statistics of mean warm cloud properties ((a) column droplet effective radius, (b) cloud liquid water path, and (c) corrected cloud albedo) as functions of LTS and AI.

variability in  $\overline{Re(column)}$  that is attributed to  $dLTS_{bin}$  for both the MODIS and GOCART cases, showing consistently that cloud droplet size is correlated better with AI than it is with LTS by using the definition (1) and (2).

[29] Figure 5b shows the variability of  $\overline{CLWP}$  as a function of NCEP LTS and AI. While higher LTS corresponds to slightly lower CLWP for all AI bins, it is clear that AI is more strongly correlated with CLWP. An increase

**Table 1.** Mean Changes in Cloud Properties With Increases in  $dAI_{95\%}$  and  $dLTS_{95\%}$ 

Forcing	$\overline{dRe(colum)}_{95\%}, \mu\text{m}$ ( $\frac{ dRe(colum) }{\overline{dRe(colum)}_{95\%}} * 100$ )		$\overline{dCLWP}_{95\%}, \text{g/m}^2$ ( $\frac{ dCLWP }{\overline{dCLWP}_{95\%}} * 100$ )		$\overline{dCCA}_{95\%}$ ( $\frac{ dCCA }{\overline{dCCA}_{95\%}} * 100$ )	
	MODIS	GOCART	MODIS	GOCART	MODIS	GOCART
$dAI_{95\%}$	-12.24 (24.4%)	-12.19 (24.3%)	-39.24 (20.8%)	-42.56 (22.6%)	0.039 (10.6%)	0.026 (7.1%)
$dLTS_{95\%}$	-8.77 (17.5%)	-8.35 (16.6%)	-8.51 (4.5%)	-5.04 (2.6%)	0.115 (31.2%)	0.117 (31.8%)

in  $dAI_{95\%}$  corresponds to a reduction of  $39.2 \text{ g/m}^2$  of  $\overline{CLWP}$  in the MODIS AI case and  $43.56 \text{ g/m}^2$  in the GOCART case, explaining 20.8% and 22.6% of  $\overline{dCLWP}_{95\%}$  ( $188.0 \text{ g/m}^2$ ) (Table 1). On the other hand, an increase in  $dLTS_{95\%}$  corresponds to a reduction of  $8.51 \text{ g/m}^2$  of  $\overline{CLWP}$  in the MODIS case and  $5.04 \text{ g/m}^2$  in the GOCART case, which explains only 4.5% and 2.6% of  $\overline{dCLWP}_{95\%}$  ( $188.0 \text{ g/m}^2$ ), respectively (Table 1). Table 2 also shows that  $\overline{CLWP}$  is more strongly correlated with the AI than it is with LTS by using the definition (2). Note that we also tested the VIRS-derived CLWP and found similar results (not shown here). *Han et al.* [1998] examined data from the Advanced Very High Resolution Radiometer (AVHRR) with the same 273 K cloud top temperature threshold for low cloud sampling, and also found that the liquid water path decreases with decreasing cloud droplet size. On the other hand, *Sekiguchi et al.* [2003] examined AVHRR data corresponding to a different low cloud top temperature threshold (below 257 K), and found that the liquid water path increases with decreasing cloud droplet size. These different results suggest that different sampling criteria in terms of cloud top temperature could be a key issue leading to qualitative differences in the relationships between liquid water path and cloud droplet size.

[30] *Twomey et al.* [1984] assumed that liquid water path remained constant as aerosol concentrations increased, while *Albrecht* [1989] hypothesized that high aerosol concentrations could increase CLWP via a less efficient precipitation process. Originally both hypotheses were built assuming that only microphysical processes affect cloud properties. The aerosol semidirect effect [*Ackerman et al.*, 2000; *Koren et al.*, 2004; *Krüger and Graßl*, 2004] is one possible reason for the low CLWP with high aerosol concentrations that we observed in this analysis. Some model studies proposed microscale dynamic processes that qualitatively explain this result. For example, *Jiang et al.* [2002], using a nonhydrostatic two-dimensional eddy-resolving model with an explicit microphysics parameterization, found that drizzle inhibition due to air pollution results in a stable boundary layer below cloud, which reduces the moisture supply and leads to low CLWP. In the clean environment, enhanced drizzle evaporation below

the cloud destabilizes the boundary layer, which results in penetrating cumuli, leading to high CLWP. These relationships must be further tested with different observations and a number of simulation studies.

[31] Finally, Figure 5c shows variations in  $\overline{CCA}$  with LTS and AI. There is a strong, linear correlation with LTS. An increase in  $dLTS_{95\%}$  corresponds to an increase of  $\overline{CCA}$  by 0.115 in the MODIS case and by 0.117 in the GOCART case, which explains 31.2% and 31.8% respectively of  $\overline{dCCA}_{95\%}$  (0.37) (Table 1). On the other hand, the AI-CCA relationship appears to be nonlinear and different between the MODIS and the GOCART cases. An increase in  $dAI_{95\%}$  corresponds to a very slight increase of  $\overline{CCA}$  (about 0.039 in the MODIS case and 0.026 in the GOCART case), and explains 10.6% and 7.1% respectively of  $\overline{dCCA}_{95\%}$  (0.37) (Table 1). For high-AI bins, CCA-AI correlation slopes are nearly zero and/or slightly negative, while positive CCA-AI correlation slopes exist for low-AI bins. Although we used CCA instead of cloud optical depth, this result is similar to that inferred from satellite measurements of cloud optical depth over the Amazon basin [*Kaufman and Fraser*, 1997]. By using the definition (2), the correlation slope of MODIS AI with CCA is comparable to the correlation of LTS with CCA (Table 2), suggesting that the aerosol-CCA correlation can be captured frequently over the globe. However, this is not captured in the GOCART case; that is, AI has a weak correlation with the CCA by using both the definition (1) and (2). We conduct further tests of these relationships on a local scale in the next section.

[32] Note that partially cloudy VIRS pixels could result in biases in the retrieved cloud properties. Cloud optical depth and cloud top temperature could have a negative bias, while cloud droplet radius can be overestimated, from a partially cloudy VIRS pixel. Variation of AI in a partially cloudy pixel can affect the values of estimated cloud properties to some degree that has not yet been quantified.

### 3.2. Local Statistics Between Cloud Properties, AI, and LTS

[33] In the previous section, we found strong relationships between cloud properties, AI, and LTS on the global

**Table 2.** Frequency Weighted Mean Values of the Change in Cloud Properties With Increases in  $dAI_{bin}$  and  $dLTS_{bin}$  Over the Globe<sup>a</sup>

Forcing	$\overline{dRe(colum)}_{freq}, \mu\text{m}$		$\overline{dCLWP}_{freq}, \text{g/m}^2$		$\overline{dCCA}_{freq}$	
	MODIS	GOCART	MODIS	GOCART	MODIS	GOCART
$dAI_{bin}$	-1.80	-1.58	-3.85	-5.04	0.0136	0.0016
$dLTS_{bin}$	-0.94	-0.85	-0.62	-0.37	0.0135	0.0133

<sup>a</sup>Changes in cloud properties are weighted by the sampling number as described in the text.

scale, and the correlation slopes are quantified by the definition (1) and (2). In this section, we examine how those relationships vary in different geographical regions. *Sekiguchi et al.* [2003] examined local correlations using the AVHRR and the POLarization and Directionality of the Earth's Reflectances (POLDER) instrument, and showed that strong correlation between aerosols and cloud properties exist along coastlines where continental air masses meet maritime clean air. We derive the linear correlation coefficient in each  $4^\circ$  box on a global grid for the same annual sampling period used in the previous section. The variability of local positive or negative correlation reported by *Sekiguchi et al.* [2003] is seen in this study to depend on both aerosol and thermodynamic variability. Positive (negative) correlations are showed in red (blue) shades, and statistically insignificant correlations (approximately,  $|r| < 0.05$ ) with t-distribution critical level set to 0.05 are shown in white (Figure 6).

[34] Figure 6a shows the correlation map between  $\text{Re}(\text{column})$  and MODIS AI (left), GOCART AI (center), and NCEP LTS (right). Strong negative correlations (blue) appear in the subtropics in the Northern Pacific Ocean, in the Indian Ocean, and in most of the Atlantic Ocean. Correlation maps for the MODIS and GOCART cases show general agreement with the global statistics discussed in section 3.1. Weak correlations (white) and slightly positive correlations (red) appear in the remote Southern Pacific Ocean in the MODIS case, in the middle of the Pacific Ocean in the GOCART case, and off the west coast of Africa. In the remote ocean, the correlation coefficient may be very small because of the small variability in AI and the low sampling number. Overall correlations are negative, which was captured in the global statistics (section 3.1). The LTS- $\text{Re}(\text{column})$  correlation also appears to be highly positive in the subtropics and weak or slightly negative in the Pacific Ocean. This is because, in subtropical regions, LTS varies substantially because of propagating midlatitude fronts and the seasonal shift of the large-scale circulation (Figure 1). These considerations also explain the weak correlation in the equatorial regions, where LTS does not change substantially throughout the year (Figure 1).

[35] Figure 6b shows the local correlation map between CLWP and MODIS AI (left), GOCART AI (center), and NCEP LTS (right). Negative correlations (blue) in the MODIS case appear in the northern subtropics in the Pacific Ocean, in the coastal zones around the Indian Ocean and South Africa, and for the northern part of the Atlantic Ocean. The GOCART case has a slightly larger area of negative correlations than the MODIS case, which is consistent with the result discussed in the previous section. The geographical locations of the negative correlations are, apparently, coherent with those of  $\text{Re}(\text{column})$  (Figure 6a). This suggests that a reduction in cloud droplet size and cloud liquid water associated with high concentrations of aerosols occurs simultaneously on a local scale over the ocean.

[36] Figure 6c shows the local correlation map between CCA and MODIS AI (left), GOCART AI (center), and NCEP LTS (right). The MODIS case shows positive correlations over almost the entire domain; that is, the aerosol indirect effect exists over almost the entire ocean. The GOCART case shows positive correlations in the northern

part of the Pacific Ocean and off the east coast of North America, while negative correlations appear off the east coast of Australia and Africa and in some remote ocean areas. This result is consistent with the global statistics; the MODIS case shows stronger correlation between AI and the CCA than the GOCART case does (section 3.1). Both the MODIS and the GOCART cases show that the strongest positive correlation appears in the Northern Pacific, where a combination of industrial and dust aerosols from East Asia advect over the ocean. LTS also has a consistently positive correlation with CCA over the global ocean.

[37] In section 3.1, we found that increases in AI as well as LTS are accompanied by decreases in cloud droplet size, decreases in liquid water path, and increases in CCA. However, in a marine environment, if AI becomes high, but LTS becomes low, changes in cloud properties can be offset or very small because of the competition between AI and LTS. *Jiang et al.* [2002] and *Takemura et al.* [2005] also found that a change in simulated CLWP could depend upon the large-scale thermodynamic feedback. In section 1, we stated that AI and LTS are independent on the global scale. In contrast, they are usually correlated either positively or negatively on a local scale (Figure 7). In the MODIS case, negative correlations appear in a large portion of the southern Pacific Ocean, and positive and negative correlations appear in the Atlantic Ocean. In the GOCART case, negative and positive correlations also appear in different regions. Positive AI-LTS correlations mean that high (low) AI appears with high (low) LTS. For positively correlated regions, both factors tend to reduce  $\text{Re}(\text{column})$  and CLWP, while increasing CCA (Figure 6). On the other hand, negative AI-LTS correlations mean that high (low) AI appears with low (high) LTS, which has the opposite effect on cloud properties (Figure 6). Comparing Figures 6 and 7, the regions with negative AI-LTS correlations are coherent with the regions with weak AI-cloud properties correlation in Figure 6, such as the southern Pacific Ocean and off the west coast of West Africa. This implies that the global distribution of local aerosol-cloud relationship could be modulated by feedback from the large-scale thermodynamic field. The importance of the large-scale feedback on aerosol direct and indirect effects is investigated and discussed in the global modeling study presented by *Takemura et al.* [2005].

### 3.3. Diurnal Cycle of Cloud Properties in Different LTS and AI Regions

[38] As introduced in section 1, marine low clouds have radiation-driven strong diurnal variability [e.g., *Driedonks and Duynkerke*, 1989]. The TRMM sun-asynchronous orbit allows us to examine the daytime diurnal cycle of  $\text{Re}(\text{column})$ , CLWP, and CCA in regions with different LTS and AI. For clarity, LTS and AI bins are assigned to be twice as large as those in the previous sections. The LTS and AI contours in the figures are labeled by the mean value of each LTS and AI bin, respectively.

[39] Figure 8a shows the daytime diurnal cycle of various cloud properties in different LTS bins.  $\text{Re}(\text{column})$  appears to be higher in lower-LTS bins, while CCA appears to be larger in higher-LTS bins over most of the diurnal cycle.  $\text{Re}(\text{column})$  reaches its maximum from 10 am to 1 pm and decreases toward evening, with consistent behavior for any

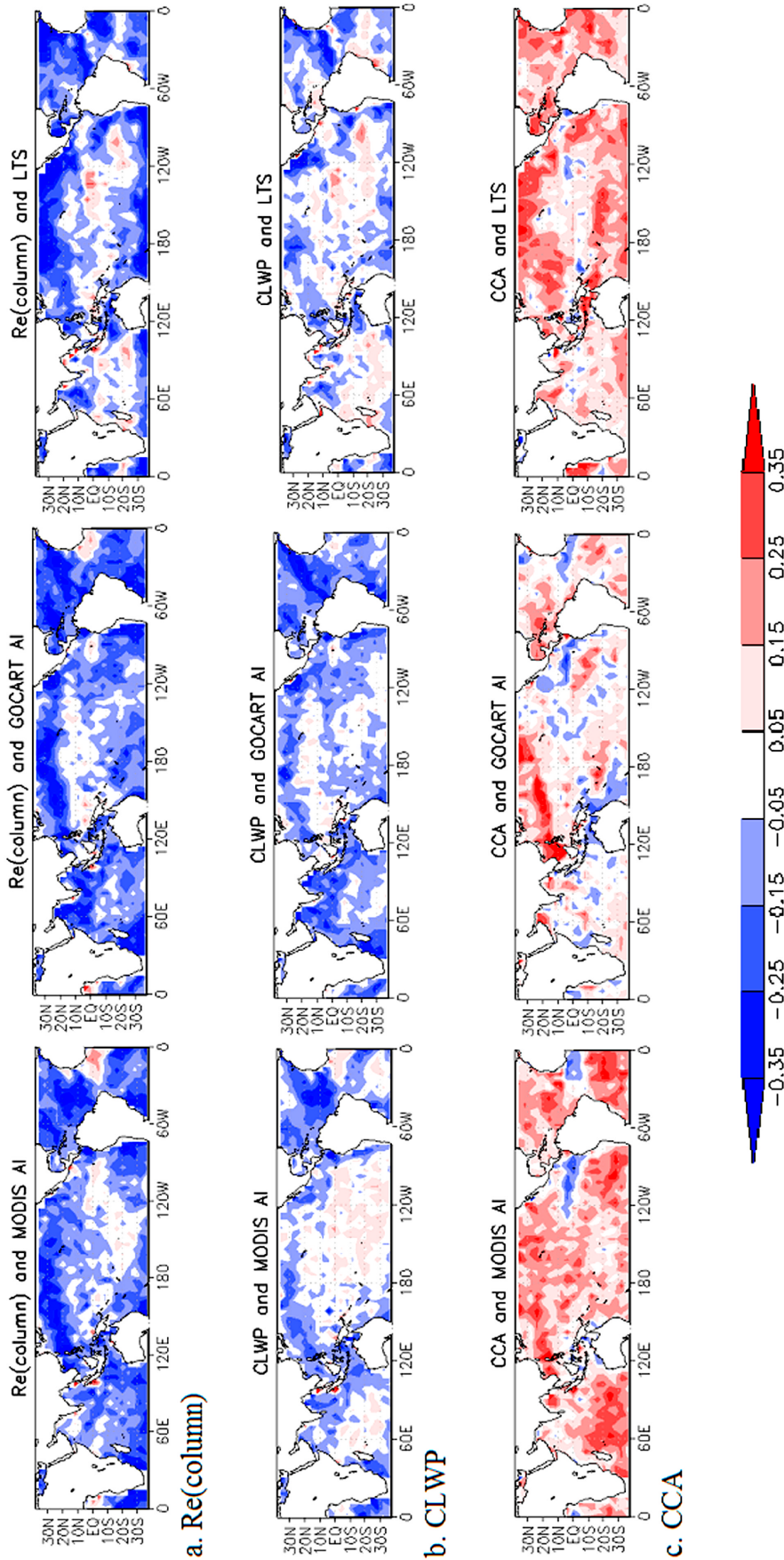


**Figure 6.** Linear correlation coefficient in each  $4^\circ$  box on a global grid for the same annual sampling period as in Figures 1 and 2. Nonsampled grids (over land) and statistically insignificant correlations (approximately,  $|r| < 0.05$ ) with the t-distribution critical level set to 0.05 are shown in white. (a) Re (columns), (b) CLWP, and (c) CCA are linearly correlated with MODIS AI, GOCART AI, and LST.

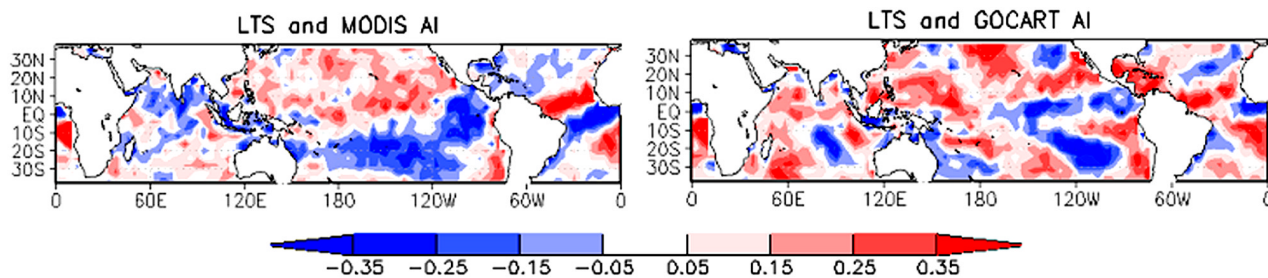


**Figure 7.** Linear correlation coefficient between AI and LTS in each  $4^\circ$  box on a global grid for the same annual sampling period as in Figure 6. Positive AI-LTS (red) correlations mean that high AI appears with high LTS, while negative AI-LTS correlations mean that high AI appears with low LTS, which has opposite effect on cloud properties. Therefore negative-correlation regions appear to be coherent with the weak-correlation regions in Figure 6.

LTS. The largest LTS regions (19.6) exhibit a slightly different pattern in  $\overline{CLWP}$  from the other regions.  $\overline{CLWP}$  stays at its maximum from 7 am to 12 pm and then rapidly decreases in the afternoon. In particular, times of peak  $\overline{CLWP}$  in high-LTS bins (highest three bins of LTS) appear to be in the early morning between 7 am and 9 am, while peak times in the lowest two LTS bins are in the late morning between 9 am and 1 pm. The diurnal cycles of cloud top height varies with LTS, but generally decline ( $\sim$  a few hundred meters) from the morning to the evening. These patterns are similar to observations from the FIRE intensive observation period [Hignett, 1991]. The diurnal cycle of  $\overline{CCA}$  depicts a strong contrast between daytime diurnal variability in high- and low-LTS regions. Higher-LTS bins tend to have larger morning/evening peaks and the largest diurnal variability. In the highest-LTS (19.6 K) regions,  $\overline{CCA}$  declines about 50% from its peak value in the morning. For all LTS bins, except the lowest (=11.2), the diurnal minima appear to be at noon. Morning maxima are slightly larger than those in the evening.

[40] Figure 8b shows the daytime cloud diurnal cycle for different AI.  $\text{Re}(\text{column})$  and  $\overline{CLWP}$  are generally higher for lower-AI (clean) environments over most of the diurnal cycle. Note that the sampling is unbiased with the background LTS values. Both the MODIS and GOCART relationships show distinctly different diurnal cycles between high- and low-AI bins. In the polluted environment cases (the highest three bins of AI),  $\text{Re}(\text{column})$  and  $\overline{CLWP}$  have sharp rises in the early morning between 7 am and 9 am in the MODIS case, and between 7 am and 12 pm in the GOCART case. On the other hand, the clean environmental cases (lowest two bins of AI) show consistently high values of  $\text{Re}(\text{column})$  and  $\overline{CLWP}$  between 7 am and 1 pm. In all the cases,  $\text{Re}(\text{column})$  and  $\overline{CLWP}$  show a rapid decrease in the late afternoon. Cloud top height gradually declines from the morning to midafternoon, and slightly increases between 3 pm and 5 pm. The diurnal cycle of cloud top height exhibits substantial diversity between the high- and low-AI regions in the GOCART case, but this feature is not seen in the MODIS case.  $\overline{CCA}$  has a strong diurnal cycle, but does not have any discernible variation with AI.

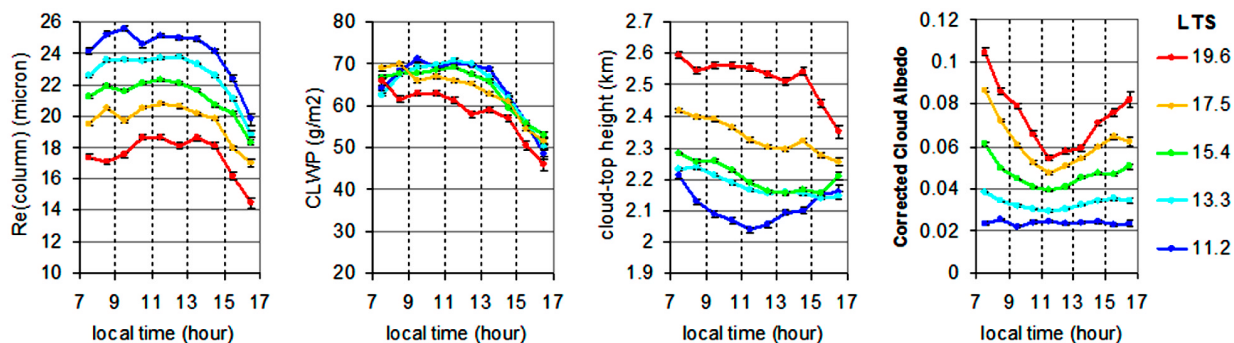
[41] While data from the TRMM satellite showed the daytime diurnal cycle of  $\text{Re}(\text{column})$ ,  $\overline{CLWP}$ , and  $\overline{CCA}$ , the exact mechanism that drives different daytime diurnal

cycles is still unknown. One possible explanation could be solar heating. As explained in section 1, absorption of solar radiation in the middle of the cloud layer and long-wave cooling at cloud top drive turbulent mixing in the cloud layer [e.g., Driedonks and Duynkerke, 1989]. The degree of solar heating may change for different droplet size spectra. Water clouds could absorb up to 15–20% of the incident solar radiation, with the largest values arising from the thickest clouds with large cloud droplets [King et al., 1990]. On the other hand, small, narrowly concentrated cloud droplet spectra tend to have less absorption of solar radiation. Therefore thin clouds with smaller droplet size forming in polluted environments could reduce evaporation due to solar heating in the morning, supporting increases the cloud droplet size and liquid water that persist later in the morning as compared with thicker clouds having larger mean droplet sizes. However, this discussion is only speculative. More intensive measurements will be required to establish the mechanisms involved.

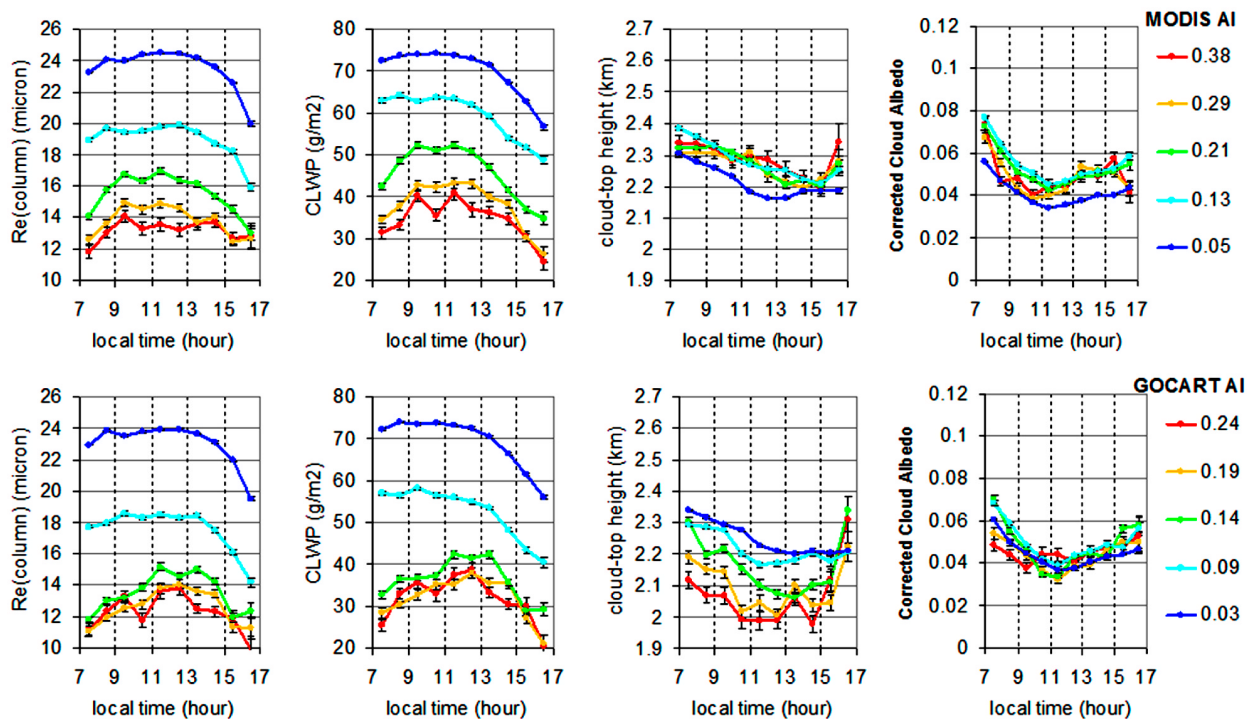
[42] An important implication of the daytime diurnal cycle is that satellite-based assessments of the aerosol indirect effect could appear to be slightly different depending on the local time of satellite overpass. Unlike the TRMM satellite, all of the polar orbiting environmental satellites (POES) have a constant local time of satellite overpass. Differences in  $\text{Re}(\text{column})$  and  $\overline{CLWP}$  between the highest-AI bin and the lowest-AI bin are largest in the early morning (Figure 8b). If one measures  $\text{Re}(\text{column})$  and  $\overline{CLWP}$  early in the morning, the correlation slope between aerosols and cloud properties could be larger than the daily mean, whereas the correlation could be smaller around noon. Moreover, the CCA-LTS correlation slope could become much larger for morning/evening-time sampling, and vice versa for noontime sampling. This daytime diurnal cycle must be incorporated into the estimation of cloud radiative forcing and the aerosol indirect effect estimated from the POES.

#### 4. Summary

[43] This study examines links between variability in marine low cloud properties derived from the TRMM satellite, MODIS/GOCART-derived aerosol index (AI), and lower-tropospheric stability (LTS) derived from the



a. Diurnal cycle of cloud properties in different LTS (K) regions



b. Diurnal cycle of cloud properties in different AI regions

**Figure 8.** Diurnal cycles of cloud properties in different (a) LTS and (b) AI regions. Contours of LTS and AI represent the mean values of the LTS and AI bins, respectively. Error bars represent standard errors ( $\sigma/\sqrt{n-2}$ , where  $n$  and  $\sigma$  are the number of quasi-coincident measurements for each bin and standard deviation, respectively).

NCEP/NCAR reanalysis. AI and LTS are used to represent column-integrated aerosol concentrations and background thermodynamic environments, respectively. Results are summarized as follows.

[44] 1. Cloud droplet sizes tend to be smallest in polluted and strong-inversion environments. Cloud droplet size decreases linearly with increasing LTS, while AI has even stronger anticorrelations with cloud droplet size, especially in clean environments. Statistical quantification shows that twice as much variability in cloud droplet size is explained by AI than by LTS.

[45] 2. Higher values of AI tend to be associated with significantly lower cloud liquid water path (CLWP), while higher LTS is linked with a slightly lower CLWP. Statistical quantification showed that the global variability of CLWP is more strongly correlated with AI than it is with LTS. These results do not support the hypotheses or assumption of constant or increased LWP of warm clouds associated with high aerosol concentrations [Twomey *et al.*, 1984; Albrecht, 1989].

[46] 3. High LTS, i.e., strong inversions, result in extensive cloud cover and high regional albedo. LTS is linearly correlated with the corrected cloud albedo (CCA: product of

cloud optical depth and cloud fraction), while the AI-CCA relationship is nonlinear and is different for the MODIS AI and the GOCART AI cases. In clean environments, small increases in AI can enhance CCA; however, this enhancement was not observed in already polluted (high-AI) environments. For the MODIS data set, statistical quantification suggests that global variability in CCA is well explained by LTS, while both AI and LTS are needed to explain local variability of CCA.

[47] 4. Most of the local correlations between AI and cloud properties agree with the results from the global statistics; that is, higher AI or higher LTS is associated with smaller cloud droplet size and lower CLWP, and higher CCA. On the other hand, weak local aerosol-cloud correlations appear in the regions where high (low) AI and low (high) LTS occur simultaneously, thereby offsetting each other.

[48] 5. Daytime diurnal cycles can explain additional variability in cloud properties; none of the cloud properties is constant through the daytime. CCA has the largest diurnal cycle in high-LTS regions, such as off the coasts of California, Namibia, and Chile. Cloud droplet size and CLWP have slightly different diurnal cycles between clean and polluted environments. Reasons for this behavior remain uncertain. This daytime diurnal cycle should be incorporated into the estimation of cloud solar radiative forcing and aerosol indirect effects produced using data from Polar Orbiting Environmental Satellites (POES).

[49] These findings should be tested with data from different satellite platforms and with various numerical modeling experiments. Remaining uncertainties and proposed future directions for analyses are summarized as follows.

[50] 1. The statistical quantification may vary for a different choice of thermodynamic (e.g., turbulent kinetic energy or updraft velocity) and aerosol parameters (e.g., AOD and the Ångström exponent derived at different wavelengths).

[51] 2. Our statistical sampling and analysis is limited to warm clouds with cloud top temperatures greater than 273 K. Analyses must be extended to ice and mixed phase clouds in future work. Such studies [e.g., *Koren et al.*, 2005; *Lin et al.*, 2006] have shown different relationships for cloud-aerosol interactions than were seen in this work.

[52] 3. Observations of the vertical distribution of AI are required on a global scale. *Kaufman et al.* [2003] proposed multisensor satellite retrievals of coarse- and fine-mode aerosol optical depth and vertical distribution by utilizing space-borne LIDAR measurements in addition to MODIS radiances in the inversion. These techniques and data sets will be available in the near future.

[53] 4. The role of GCCN is largely ignored by the use of AI as the aerosol variable. A study examining the role of GCCN more explicitly is possible by investigating the relative roles of the fine- and coarse-mode aerosol fractions available in the MODIS aerosol products.

[54] 5. The VIRS footprint size may be too coarse to resolve the properties of highly broken clouds, leading to unknown biases in the quantitative analysis. The TMI-VIRS combined algorithm used in this study can be applied to the combination of the Advanced Microwave Scanning Radiometer (AMSR) and MODIS sensors on the Aqua satellite

platform. MODIS has a much smaller footprint than VIRS, while AMSR has microwave channels similar to those of TMI.

## Notation

AI	Aerosol index: the product of aerosol optical depth and the Ångström exponent.
$dAI_{95\%}$	95% of the most frequent AI out of total probability density function (0.41 for MODIS; 0.26 for GOCART).
$dAI_{bin}$	Size of sampling bin: 10% of $dAI_{95\%}$ (0.04 for MODIS, 0.026 for GOCART).
LTS	Lower-tropospheric stability (or inversion strength): potential temperature at 700 mb – surface potential temperature.
$dLTS_{95\%}$	95% of the most frequent LTS out of total probability density function (10.5 K).
$dLTS_{bin}$	Size of sampling LTS bin: 10% of $dLTS_{95\%}$ (1.05 K).
$Re(column)$	Column integrated cloud droplet effective radius ( $\mu\text{m}$ ).
$dRe(column)_{95\%}$	A range of 95% of the most frequent ( $\approx 4\sigma$ ) $Re(column)$ out of total probability density function (50.0 $\mu\text{m}$ ).
$\overline{Re(column)}$	$Re(column)$ averaged for each bin ( $dAI_{bin}$ and $dLTS_{bin}$ ).
$\overline{dRe(column)}_{95\%}$	Mean change in $\overline{Re(column)}$ with increase in $dAI_{95\%}$ and $dLTS_{95\%}$ .
$\overline{dRe(column)}_{freq}$	Frequency weighted mean values of the change in $\overline{Re(column)}$ with increase in $dAI_{bin}$ and $dLTS_{bin}$ over the globe.
CLWP	Cloud liquid water path ( $\text{g}/\text{m}^2$ ).
$dCLWP_{95\%}$	A range of 95% of the most frequent ( $\approx 4\sigma$ ) CLWP values out of total probability density function (188.0 $\text{g}/\text{m}^2$ ).
$\overline{CLWP}$	CLWP averaged for each bin ( $dAI_{bin}$ and $dLTS_{bin}$ ).
$\overline{dCLWP}_{95\%}$	Mean change in $\overline{CLWP}$ with increase in $dAI_{95\%}$ and $dLTS_{95\%}$ .
$\overline{dCLWP}_{freq}$	Frequency weighted mean values of the change in $\overline{CLWP}$ with increase in $dAI_{bin}$ and $dLTS_{bin}$ over the globe.
CCA	Corrected cloud albedo: the product of cloud optical depth and cloud fraction in $1^\circ$ box.
$dCCA_{95\%}$	A range of 95% of the most frequent ( $\approx 4\sigma$ ) CCA out of total probability density function (0.37).
$\overline{CCA}$	CCA averaged for each bin ( $dAI_{bin}$ and $dLTS_{bin}$ ).
$\overline{dCCA}_{95\%}$	Mean change in $\overline{CCA}$ with increase in $dAI_{95\%}$ and $dLTS_{95\%}$ .
$\overline{dCCA}_{freq}$	Frequency weighted mean values of the change in $\overline{CCA}$ with increase in $dAI_{bin}$ and $dLTS_{bin}$ over the globe.

[55] **Acknowledgments.** This work is funded by NASA CEAS fellowship, NAG5-12105, and NASA Radiation Project, NNG04GB87G. VIRS (1B01) and TMI (1B11) data were provided by NASA GSFC DAAC. T. Jackson, H. Rui, J. R. Vanderpool, and W. Berg helped the author to read the tape-archived TRMM data set. NCEP/NCAR Reanalysis data were provided by NOAA CDC. The authors would like to thank T.Y. Nakajima

at NASDA/EORC for providing the GTR 4.1 packages; NASA GSFC code 613.1 Mesoscale Atmospheric Processes Branch for providing computer resources; Bill Cotton for the notes from the “Thermodynamics and Cloud Physics” course at Department of Atmospheric Science, Colorado State University; and a reviewer for his/her detailed comments and suggestions.

## References

- Ackerman, A. S., O. B. Toon, D. E. Stevens, A. J. Heymsfield, V. Ramanathan, and E. J. Welton (2000), Reduction of tropical cloudiness by soot, *Science*, **288**, 1042–1047.
- Albrecht, B. A. (1989), Aerosols, cloud microphysics, and fractional cloudiness, *Science*, **245**, 1227–1230.
- Anderson, T. L., R. J. Charlson, D. M. Winker, J. A. Ogren, and K. Holmén (2003), Mesoscale variations of tropospheric aerosols, *J. Atmos. Sci.*, **60**(1), 119–136.
- Betts, A. K. (1990), Diurnal variation of California coastal stratocumulus from two days of boundary layer soundings, *Tellus, Ser. A*, **42**, 302–304.
- Bréon, F.-M., D. Tanré, and S. Generoso (2002), Aerosol effect on cloud droplet size monitored from satellite, *Science*, **295**, 834–838.
- Chin, M., P. Ginoux, S. Kinne, O. Torres, B. N. Holben, B. N. Duncan, R. V. Martin, J. A. Logan, A. Higurashi, and T. Nakajima (2002), Tropospheric aerosol optical thickness from the GOCART model and comparisons with satellite and sunphotometer measurements, *J. Atmos. Sci.*, **59**, 461–483.
- Chin, M., D. A. Chu, R. Levy, L. A. Remer, Y. J. Kaufman, B. N. Holben, T. Eck, and P. Ginoux (2004), Aerosol distribution in the northern hemisphere during ACE-Asia: Results from global model, satellite observations, and sunphotometer measurements, *J. Geophys. Res.*, **109**, D23S90, doi:10.1029/2004JD004829.
- Cieselski, P. E., W. H. Schubert, and R. H. Johnson (2001), Diurnal variability of the marine boundary layer during ASTEX, *J. Atmos. Sci.*, **58**(16), 2355–2376.
- Driedonks, A. G. M., and P. G. Duynkerke (1989), Current problems in the stratocumulus-topped atmospheric boundary layer, *Boundary Layer Meteorol.*, **46**, 275–303.
- Dunion, J. P., and C. S. Velden (2004), The impact of the Saharan air layer on Atlantic tropical cyclone activity, *Bull. Am. Meteorol. Soc.*, **85**(3), 353–365.
- Feingold, G., W. R. Cotton, S. M. Kreidenweis, and J. T. Davis (1999), The impact of giant cloud condensation nuclei on drizzle formation in stratocumulus: Implications for cloud radiative properties, *J. Atmos. Sci.*, **56**(24), 4100–4117.
- Feingold, G., W. L. Eberhard, D. E. Veron, and M. Previdi (2003), First measurements of the Twomey indirect effect using ground-based remote sensors, *Geophys. Res. Lett.*, **30**(6), 1287, doi:10.1029/2002GL016633.
- Han, Q., W. B. Rossow, J. Chou, and R. Welch (1998), Global survey of the relationship of cloud albedo and liquid water path with droplet size using ISCCP, *J. Clim.*, **11**, 1516–1528.
- Hartmann, D. L., M. E. Ockert-Bell, and M. L. Michelsen (1992), The effect of cloud type on Earth’s energy balance: Global analysis, *J. Clim.*, **5**, 1281–1304.
- Hignett, P. (1991), Observations of diurnal variation in a cloud-capped marine boundary layer, *J. Atmos. Sci.*, **48**(12), 1474–1482.
- Hobbs, P. V. (1993), *Aerosol-Cloud Interactions*, 235 pp., Elsevier, New York.
- Jiang, H., G. Feingold, and W. R. Cotton (2002), Simulations of aerosol-cloud-dynamical feedbacks resulting from entrainment of aerosol into the marine boundary layer during the Atlantic Stratocumulus Transition Experiment, *J. Geophys. Res.*, **107**(D24), 4813, doi:10.1029/2001JD001502.
- Kalnay, E., et al. (1996), The NCEP/NCAR 40-year reanalysis project, *Bull. Am. Meteorol. Soc.*, **77**, 437–471.
- Kaufman, Y. J., and R. S. Fraser (1997), The effect of smoke particles on clouds and climate forcing, *Science*, **277**, 1636–1639.
- Kaufman, Y. J., D. Tanré, and O. Boucher (2002), A satellite view of aerosols in the climate system, *Nature*, **419**, 215–223.
- Kaufman, Y. J., D. Tanré, J.-F. Léon, and J. Pelon (2003), Retrievals of profiles of fine and coarse aerosols using lidar and radiometric space measurements, *IEEE Trans. Geosci. Remote Sens.*, **41**(8), 1743–1754.
- Kaufman, Y. J., I. Koren, L. A. Remer, D. Rosenfeld, and Y. Rudich (2005), The effect of smoke, dust and pollution aerosol on shallow cloud development over the Atlantic Ocean, *Proc. Natl. Acad. Sci.*, **102**(32), 11,207–11,212.
- Kawamoto, K., T. Nakajima, and T. Y. Nakajima (2001), A global determination of cloud microphysics with AVHRR remote sensing, *J. Clim.*, **14**, 2054–2068.
- King, M. D., L. F. Radke, and P. V. Hobbs (1990), Determination of the spectral absorption of solar radiation by marine stratocumulus clouds from airborne measurements within clouds, *J. Atmos. Sci.*, **47**(7), 894–907.
- Klein, S. A. (1997), Synoptic variability of low-cloud properties and meteorological parameters in the subtropical trade wind boundary layer, *J. Clim.*, **10**(8), 2018–2039.
- Klein, S. A., and D. L. Hartmann (1993), The seasonal cycle of low stratiform clouds, *J. Clim.*, **6**, 1587–1606.
- Koren, I., Y. J. Kaufman, L. A. Remer, and J. V. Martins (2004), Measurement of the effect of Amazon smoke on inhibition of cloud formation, *Science*, **303**, 1342–1345.
- Koren, I., Y. J. Kaufman, D. Rosenfeld, L. A. Remer, and Y. Rudich (2005), Aerosol invigoration and restructuring of Atlantic convective clouds, *Geophys. Res. Lett.*, **32**, L14828, doi:10.1029/2005GL023187.
- Krüger, O., and H. Grafl (2004), Albedo reduction by absorbing aerosols over China, *Geophys. Res. Lett.*, **31**, L02108, doi:10.1029/2003GL019111.
- Lau, K. M., and H. T. Wu (2003), Warm rain processes over tropical oceans and climate implications, *Geophys. Res. Lett.*, **30**(24), 2290, doi:10.1029/2003GL018567.
- Lin, J. C., T. Matsui, R. A. Pielke Sr., and C. Kummerow (2006), Effects of biomass burning-derived aerosols on precipitation and clouds in the Amazon Basin: A satellite-based empirical study, *J. Geophys. Res.*, doi:10.1029/2005JD006884, in press.
- Masunaga, H., T. Y. Nakajima, T. Nakajima, M. Kachi, R. Oki, and S. Kuroda (2002a), Physical properties of maritime low clouds as retrieved by combined use of Tropical Rainfall Measurement Mission Microwave Imager and Visible/Infrared Scanner: Algorithm, *J. Geophys. Res.*, **107**(D10), 4083, doi:10.1029/2001JD000743.
- Masunaga, H., T. Y. Nakajima, T. Nakajima, M. Kachi, and K. Suzuki (2002b), Physical properties of maritime low clouds as retrieved by combined use of Tropical Rainfall Measuring Mission (TRMM) Microwave Imager and Visible/Infrared Scanner 2. Climatology of warm clouds and rain, *J. Geophys. Res.*, **107**(D19), 4367, doi:10.1029/2001JD001269.
- Matsui, T., H. Masunaga, R. A. Pielke Sr., and W.-K. Tao (2004a), Impact of aerosols and atmospheric thermodynamics on cloud properties within the climate system, *Geophys. Res. Lett.*, **31**, L06109, doi:10.1029/2003GL019287.
- Matsui, T., S. M. Kreidenweis, R. A. Pielke Sr., B. Schichtel, H. Yu, M. Chin, D. A. Chu, and D. Niyogi (2004b), Regional comparison and assimilation of GOCART and MODIS aerosol optical depth across the eastern U.S., *Geophys. Res. Lett.*, **31**, L21101, doi:10.1029/2004GL021017.
- Nakajima, T., A. Higurashi, K. Kawamoto, and J. E. Penner (2001), A possible correlation between satellite-derived cloud and aerosol microphysical parameters, *Geophys. Res. Lett.*, **28**, 1171–1174.
- National Research Council (2005), *Radiative Forcing of Climate Change: Expanding the Concept and Addressing Uncertainties*, Natl. Acad. Press, Washington, D. C.
- Park, S., and C. B. Leovy (2004), Marine low-cloud anomalies associated with ENSO, *J. Clim.*, **17**, 3448–3469.
- Penner, J. E., X. Dong, and Y. Chen (2004), Observational evidence of a change in radiative forcing due to the indirect aerosol effect, *Nature*, **427**, 231–234.
- Ramanathan, V., P. J. Crutzen, J. T. Kiehl, and D. Rosenfeld (2001), Aerosols, climate, and the hydrological cycle, *Science*, **294**, 2119–2124.
- Remer, L. A., et al. (2005), The MODIS aerosol algorithm, products and validation, *J. Atmos. Sci.*, **62**(4), 947–973.
- Rosenfeld, D. (1999), TRMM observed first direct evidence of smoke from forest fire inhibiting rainfall, *Geophys. Res. Lett.*, **26**, 3105–3108.
- Sekiguchi, M., T. Nakajima, K. Suzuki, K. Kawamoto, A. Higurashi, D. Rosenfeld, I. Sano, and S. Mukai (2003), A study of the direct and indirect effects of aerosols using global satellite data sets of aerosol and cloud parameters, *J. Geophys. Res.*, **108**(D22), 4699, doi:10.1029/2002JD003359.
- Slingo, A. J. (1990), Sensitivity of the Earth’s radiation budget to changes in low clouds, *Nature*, **343**, 49–50.
- Stephens, G. L., et al. (2002), The CloudSat mission and the A-train: A new dimension of space-based observations of clouds and precipitation, *Bull. Am. Meteorol. Soc.*, **83**, 1771–1790, doi:10.1175/BAMS-83-12-1771.
- Takemura, T., T. Nozawa, S. Emori, T. Y. Nakajima, and T. Nakajima (2005), Simulation of climate response to aerosol direct and indirect effects with aerosol transport-radiation model, *J. Geophys. Res.*, **110**, D02202, doi:10.1029/2004JD005029.
- Twomey, S., M. Piepgrass, and T. L. Wolfe (1984), An assessment of the impact of pollution on global cloud albedo, *Tellus, Ser. B*, **36**, 356–366.

- Weare, B. C. (1994), Interrelationships between cloud properties and sea surface temperatures on seasonal and interannual time scales, *J. Clim.*, 7(2), 248–260.
- Wood, R., C. S. Bretherton, and D. L. Hartmann (2002), Diurnal cycle of liquid water path over the subtropical and tropical oceans, *Geophys. Res. Lett.*, 29(23), 2092, doi:10.1029/2002GL015371.
- Yu, H., R. E. Dickinson, M. Chin, Y. J. Kaufman, B. N. Holben, I. V. Geogdzhayev, and M. I. Mishchenko (2003), Annual cycle of global distributions of aerosol optical depth from integration of MODIS retrievals and GOCART model simulations, *J. Geophys. Res.*, 108(D3), 4128, doi:10.1029/2002JD002717.
- 
- M. Chin, Y. J. Kaufman, and W.-K. Tao, Laboratory for Atmospheres, NASA Goddard Space Flight Center, Greenbelt, MD 20771, USA.
- S. M. Kreidenweis, H. Masunaga, T. Matsui, and R. A. Pielke Sr., Department of Atmospheric Science, Colorado State University, Fort Collins, CO 80523-1371, USA. (matsuit@atmos.colostate.edu)